Electronic Supplementary Information

Highly Ordered Multi-layered Hydrogenated TiO_2-II phase Nanowire Arrays Negative Electrode for 2.4 V Aqueous Asymmetric Supercapacitors with High Energy Density and Long Cycle Life

Yongfu Tang [a, b *], Yanshuai Li [a], Wenfeng Guo [a, c], Jing Wang [a], Xiaomei Li [a], Shunji Chen [a], Shichun Mu [d, *], Yufeng Zhao [a], Faming Gao [a]

[a] Hebei Key Laboratory of Applied Chemistry, College of Environmental and Chemical Engineering, Yanshan University, Qinhuangdao, 066004, China

[b] Key Laboratory of Preparation and Application of Environmental Friendly Materials (Jilin Normal University), Ministry of Education, Changchun, 130103, China

[c] State Key Laboratory of Metastable Materials Science and Technology, Yanshan University, Qinhuangdao, 066004, China

[d] State Key Laboratory of Advanced Technology for Materials Synthesis and Processing, Wuhan University of Technology, Wuhan, 430070, China

1 Experimental section

1.1 Preparation of the ML-HTO electrode

1.1.1 Preparation of the pristine TO electrode

The pristine binder-free self-supported TO nanowire arrays were prepared by a two step including a chemical oxidation process. Firstly, the 2.0 cm × 0.5 cm titanium foils with a thickness of 0.1 mm were cleaned by ultrasonic processing in acetone and ethanol for 20 min, respectively. The cleaned titanium foils were then immersed in a

*Corresponding author. Tel.: +86 13780351724
E-mail address: tangyongfu@ysu.edu.cn (Y. Tang), msc@whut.edu.cn (S. Mu)

mixed pickling solution which was composed of hydrofluoric acid (5.0 wt. %) and nitric acid (16.3 wt. %) for 2 min. The pickled titanium foils were washed in deionized water for 30 min. In the chemical oxidation process, several cleaned titanium foils were immersed in 30 ml of hydrogen peroxide solution (30 wt. %), including 60 mg of melamine and 1 ml of nitric acid (60 wt. %), and then were reacted at 80 ^{o}C for 48 h. After cooling to room temperature, the obtained foils were washed with deionized water and finally dried in air to obtain the pristine TO electrode.

1.1.2 Preparation of the HTO and ATO electrode

The obtained pristine TO electrodes were pyrolysized at 300 ^{o}C in a tubular furnace with H_2 flow for 1 h to obtain the titanium supported hydrogenated TiO_2 nonawire arrays electrode, which was denoted as the HTO electrode.

For comparison, another electrodes were obtained via the pyrolysis of the TO electrode at 300 ^{o}C in the tubular furnace in air atmosphere for 1 h and denoted as ATO electrode to investigate the effect of the hydrogenation process on the structure and electrochemical properties of the electrode.

1.1.3 Preparation of the ML-HTO electrode

The as-prepared HTO electrodes above were put into a Teflon-lined stainless steel autoclave with 50 ml 0.05 M glucose solution and kept at 180 ^{o}C for 24 h. After cooling to room temperature, the products were washed with deionized water and finally dried in air to obtain the carbon coating HTO electrode. Then, the carbon coating HTO electrodes were immersed into the mixed solution of 30 ml hydrogen

peroxide solution (30 wt. %), 60 mg melamine, 1 ml nitric acid (60 wt. %). Several cleaned titanium foils were also added into the solution as the titanium source. And then were heated at 80 ^{o}C for 48 h after sealing with plastic wrap. The samples were rinsed with deionized water and dried at room temperature. The prepared electrodes were pyrolysized at 300 ^{o}C in a tubular furnace with H_2 flow for 1 h to obtain the carbon coating 3D multi-layered hydrogenated TiO_2 nanowires electrode, which was denoted as the ML-HTO electrode. For comparison, the TL-HTO electrode was prepared similar to the ML-HTO electrode just without the hydrothermal carbon coating process to obtain the carbon coating transition layer.

1.2 Physicochemical characterization of the as-prepared electrodes

The phase structure of all the functional layers in the electrodes were characterized by X-ray diffraction (XRD, Bruker AXS D8 diffractometer with Cu K_α Rradiation with λ of 0.15418 nm) with angle scan rate of 3^{o}/min. To avoid the influence of the Ti substrate on the active materials, all the XRD patterns were performed on the active materials peeled from the electrodes. The grain size of the TiO_2 active materials was calculated via Scherrer equation as $D = \frac{K\gamma}{B\cos\theta}$, where the D, K, γ, B and θ represent for the mean grain size at a specific facet corresponding to a diffraction angle of θ, the Scherrer constant, the wave length of X-ray, the peak width at half height and the diffraction angle, respectively.

The morphology of the electrodes were characterized by field emission scanning electron microscopy (FESEM, SUPRA55,□Carl Zeiss Corp., Germany), transmission electron microscopy (TEM, HT7700, Hitachi Corp., Japan, 100 kV, 10 μA) and high-

resolution TEM (HRTEM, JEM 2010 model, JEOL Ltd. Corp., Japan). A drop of slurry, uniformly suspended in ethanol, was dispersed on the amorphous carbon film supported on Cu grid for TEM and HRTEM analysis. The UV-visible adsorption spectra of the active materials in the as-prepared electrodes were conducted in $BaSO_4$ pellets by adsorption mode with the UV-2550 instrument. Raman spectra of the active materials peeled from the electrodes were measured by a Raman station 400 F instrument. The surface states of the active materials in the as-prepared electrodes were analyzed by X-ray photoelectron spectroscopy (XPS) measurements.

1.3 Electrochemical measurements of the as-prepared electrodes

The electrochemical properties of all electrodes were evaluated by cyclic voltammetry (CV) and galvanostatic charge-discharge (GC) based on the CHI 604E electrochemical station (CH Instruments Corp., Shanghai, China) and Land CT 2001A instruments (Land Instruments Corp., Wuhan, China), respectively. The CV measurements were performed by the typical three-electrode system, all the prepared electrodes were measured as the working electrode. Both the CV and the GC measurements were conducted in the 0.5 M Na_2SO_4 solution. The 1×1 cm^2 Pt foil and the saturated calomel electrode (SCE) were used as the counter electrode and the reference electrode, respectively. The mean specific capacitance of the electrode was calculated as $C = \int I\mathrm{d}t / m\Delta V$, where I, m, t and ΔV are the galvanostatic current density, the mass of active material, the discharge time and the potential window, respectively. The electrochemical impedance spectroscopy (EIS) of all working electrodes were also conducted by CHI 604E electrochemical station. The frequency

range and amplitude of the EIS measurement are 0.05 Hz~100 kHz and 5 mV, respectively. The EIS measurement was performed at open circuit potential without bias potential.

The Mott-Schottcky plots of the electrodes were generated based on capacitances that were derived from the electrochemical impedance obtained at each potential with 1.0 kHz frequency in the dark. The Na^+ ion diffusion coefficients on different electrodes were calculated according to $D = \frac{R^2T^2}{2A^2n^4F^4C^2\sigma^2}$, where R is the gas constant (8.314 J K^{-1} mol^{-1}), T is the room temperature (298.15 K), A is the surface area of the electrode, n is the number of electrons transferred based on **Eqs. 1 or 2** [3], F is the Faraday constant (96 485 C mol^{-1}), C is the concentration of Na^+ (1.0 M), and σ is the slope of the plot of Z_{re} against $\omega^{-1/2}$ based on $Z_{re} = R_s + R_{ct} + \sigma\omega^{-1/2}$, where the Z_{re}, R_s and R_{ct} represent for the real axis of Nyquist plots, the ohmic resistance and charge transfer resistance, respectively.

1.4 Fabrication and measurements of MnO_2//ML-HTO supercapacitor

The MnO_2//ML-HTO ASCs were assembled with the home made MnO_2 coated carbon cloth as the positive electrode and the ML-HTO as the negative electrode with a cellulose based separator. The MnO_2 active materials was prepared via a facile method as follow: 1.5 g sucrose dissolved in 30 mL deioned water was mixed with 0.3 g $KMnO_4$ dissolved in 30 mL deioned water. The mixed solution was stirred on the magnetic stirrer for 14 h at room temperature. Then, the MnO_2 active material was finally obtained after centrifuging, washing, and vacuum drying. The MnO_2 active material coated carbon cloth (CC) positive electrode was prepared via coating the

MnO_2 slurry on the CC. The slurry was composed of MnO_2, polyvinylidene fluoride (PVDF) and acetylene black (AB) with the mass ratio of MnO_2:PVDF:AB = 8:1:1 and uniformly dispersed in the N-methyl-2-pyrrolidone (NMP). The coated CC was dried at 80 oC for 12 to obtain the final MnO_2 based positive electrode. The mass loading of the active materials in the positive electrode were 4.0 mg cm^{-2}, in order to balance the charges between the electrodes based on **Eq. S1**. A 0.5 M Na_2SO_4 aqueous solution was employed as the electrolyte.

$$C_+ \cdot m_+ = C_- \cdot m_- \qquad \text{(S1)}$$

Where C_+, m_+, C_- and m_- are the capacity (mAh g^{-1}) of positive electrode, mass loading (g) of positive electrode, capacity of negative electrode and mass loading of negative electrode. The mean specific capacitance of the as-prepared MnO_2//ML-HTO ASCs was calculated as $C = \int I\mathrm{d}t / m\Delta V$, where I, m, t and ΔV are the galvanostatic current density, the total mass of active material in both positive and negative electrodes, the discharge time and the voltage window, respectively.

2. Supplementary Tables

Table S1 The ratios of the Ti^{3+} and Ti^{4+} species in the total Ti species, as well as the Ti-O-Ti, Ti-OH and adsorbed H_2O species in the total O species based on the integration of the deconvoluted peaks in the TO, ATO, HTO and ML-HTO electrodes.

Electrodes	Ti species		O species		
	Ti^{3+}	Ti^{4+}	Ti-O-Ti	Ti-OH	$(H_2O)_{ad}$
TO	0	100 %	----	----	----
ATO	0	100 %	60.1 %	39.9 %	0
HTO	38.5 %	61.5 %	50.9 %	43.8 %	5.3 %
ML-HTO	39.8 %	60.2 %	33.1 %	56.6 %	10.3 %

Table S2 Comparison of cell voltages and mass specific energy densities based on various aqueous asymmetric supercapacitors with high cell voltages.

Positive electrode	Negative electrode	Electrolyte	Cell voltage (V)	E(Wh kg^{-1})	P(W kg^{-1})	Ref
MnO_2	ML-HTO	0.5 M Na_2SO_4	**2.4**	**90.3**	349.0	This work
MnO_2	Graphene	0.5 M Na_2SO_4	2.0	23.2	1000	[42]
MnO_2	AC	1.0 M Na_2SO_4	2.0	17.1	100	[43]
MnO_2/GHCS	GHCS	1.0 M Na_2SO_4	2.0	22.1	100	[44]
MnO_2/CNF	ACNF	0.5 M Na_2SO_4	2.0	30.6	200	[45]
MnO_2/GC	Graphene	1.0 M Na_2SO_4	2.0	30.4	100	[46]
MnO_2/MWCNTs	AC	0.5 M Li_2SO_4	1.8	17.8	400	[47]
p-BC@MnO_2	p-BC/N	1.0 M Na_2SO_4	2.0	32.9	200	[48]
MnO_2-ERGO	CNT-ERGO	1.0 M KCl	1.8	31.8	453.6	[49]
aMEGO/MnO_2	aMEGO	1.0 M Na_2SO_4	2.0	24.3	24500	[50]
Carbon	Carbon	1.0 M Na_2SO_4	1.8	12.7	100	[51]

Table S3 Comparison of volumetric specific energy densities based on various aqueous asymmetric supercapacitors evaluated by volumetric specific energy density.

Positive electrode	Negative electrode	Electrolyte	E(mWh cm^{-3})	P(mW cm^{-3})	Ref
MnO_2	ML-HTO-NWAs @C/Ti	0.5 M Na_2SO_4	9.6	61	This work
H-TiO_2@MnO_2	H-TiO_2@C	5.0 M LiCl	0.45	~200	[28]
H-TiO_2@MnO_2	H-TiO_2@C	LiCl/PVA	0.3	~180	[28]
H-MnO_2	RGO	LiCl/PVA	0.25	1000	[52]
VO_x	VN	LiCl/PVA	0.61	800	[53]
Fe_2N	TiN	LiCl/PVA	0.51	211.4	[54]

All the references in **Tables S2** and **S3** are given in the manuscript.

3. Supplementary Figures

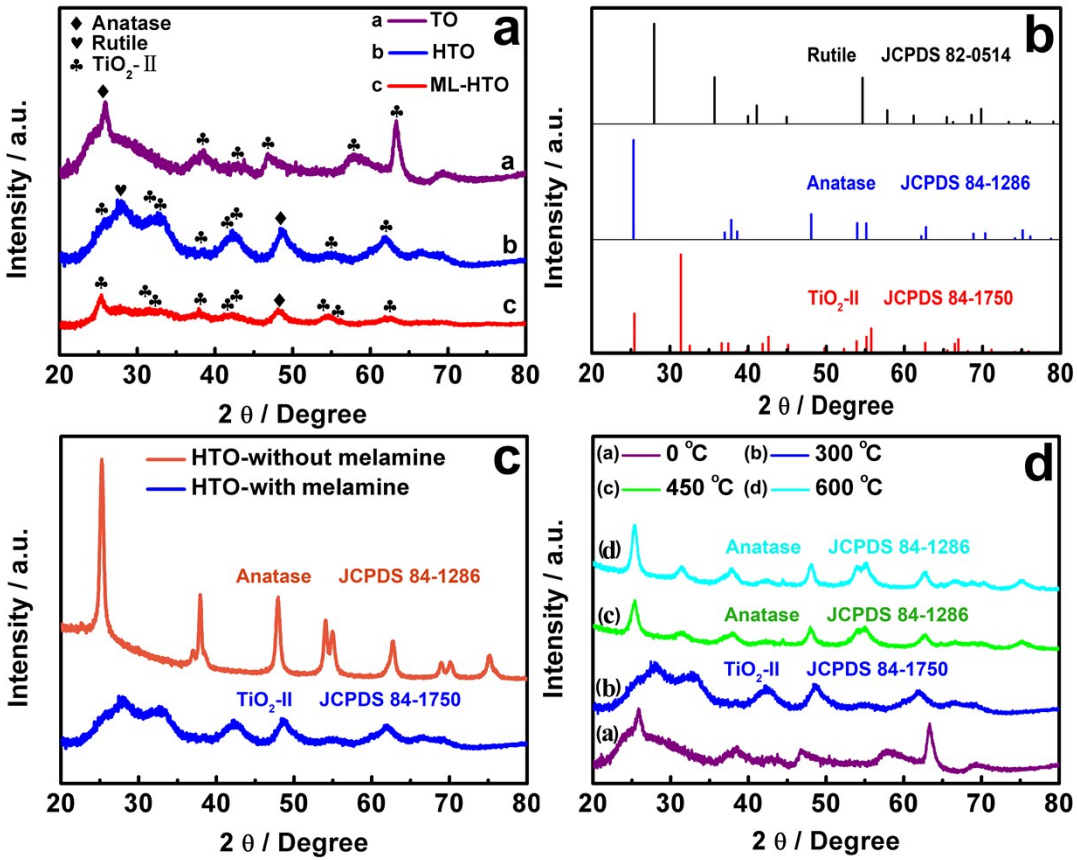

Figure S1 (a) XRD patterns of the active materials peeled from the TO, HTO and ML-HTO electrodes, respectively. (b) JCPDS cards for rutile, anatase and TiO_2-II phases of TiO_2. (c) Comparison for XRD patterns of the pristine TO electrodes prepared with and without melamine as the additives. (d) Comparison for XRD patterns of the HTO electrodes pyrolysised at different temperature.

As shown in **Figure S1a**, the diffraction peaks attributed to the TiO_2-II phase are observed in all the electrodes. The detection of TiO_2-II phase in the pristine TO electrode indicates that the high pressure α-PbO_2 type TiO_2-II phase has been formed in the melamine-assisted chemical oxidation process, which was the first time to obtain a TiO_2-II phase in a mild ambience without high pressure to the best of our

knowledge [1-2]. After hydrogenation at 300 ^{o}C, the phase purity and the crystallinity of the TiO_2-II phase in the HTO electrode becomes higher. The XRD patterns of the similar HTO electrodes prepared via the chemical oxidation method with (a line) and without (b line) melamine are shown in **Figure S1c** to investigate the effect of the melamine on the formation of the TiO_2-II phases in the TiO_2 NWAs. As shown, only diffraction peaks attributed to anatase TiO_2 phase are observed in the electrode obtained without the melamine in the chemical oxidation process. This result indicates that the melamine play important roles in the formation of TiO_2-II phase, although the mechanism should be further investigated. The XRD patterns of the TiO_2 NWAs electrodes pyrolysized at different temperatures are also investigated to demonstrates the effect of the pyrolysis temperature on the phase structure of the TiO_2 NWAs electrodes. As shown in **Figure S1d**, the TiO_2-II phase is transformed into anatase when the temperature was higher than 400 ^{o}C. In summary, the high pressure TiO_2-II phase is formed during the melamine-assisted chemical oxidation and can be kept in low temperature (300 ^{o}C) pyrolysis.

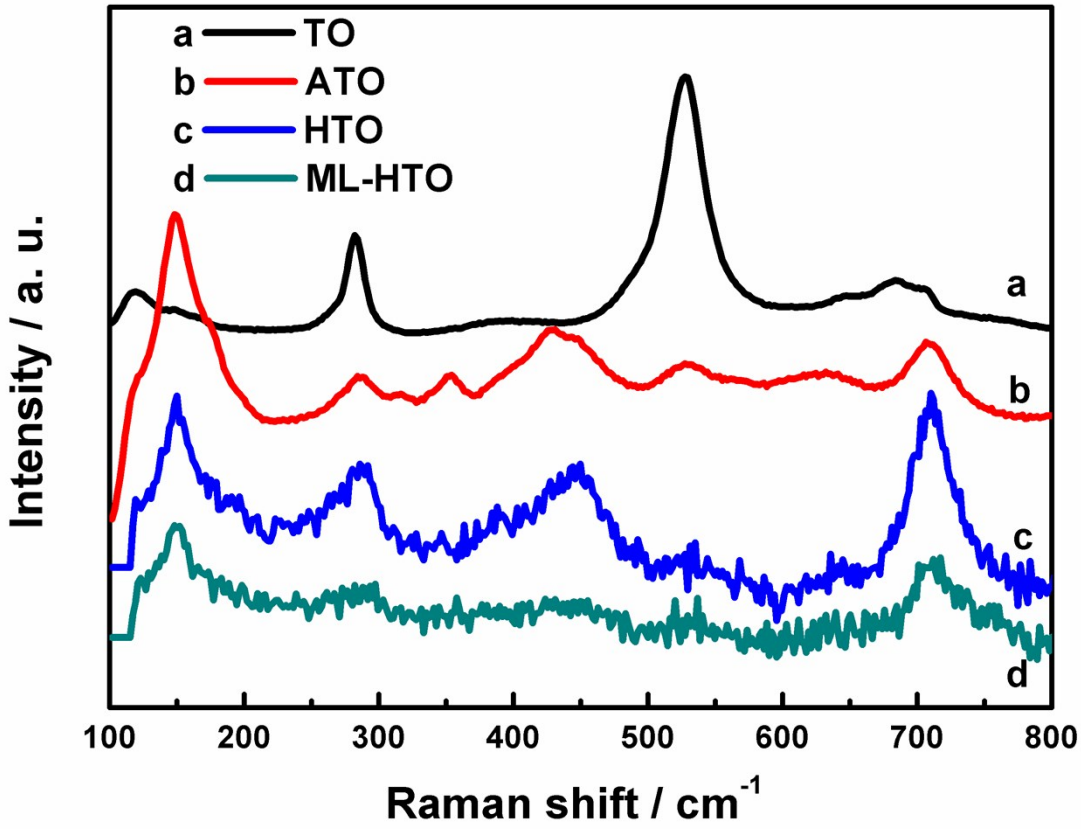

Figure S2 Raman spectra of the active materials in the TO, ATO, HTO and ML-HTO electrodes

As shown, the comparison for the Raman spectroscopy of the TO, ATO, HTO and ML-HTO electrodes are given in **Figure S2**. As shown, the smooth peaks observed in the Raman spectroscopy of the TO and ATO electrodes imply the high signal-to-noise ratio for the measurements of Raman spectroscopy here. The peaks located at at the wave number of 151, 171, 291, 359, 445, 520, 539, 631 and 812 cm^{-1} are attributed to the vibration of the $2B_{3g} + 3B_{2g} + 3B_{2g} + 1A_g$ modes of the TiO_2-II phase. The clear broadening of Raman peaks in the ML-HTO and HTO electrodes should be attributed to the introduction of oxygen vacancy defects in TiO_2-II phase during the hydrogenation process.

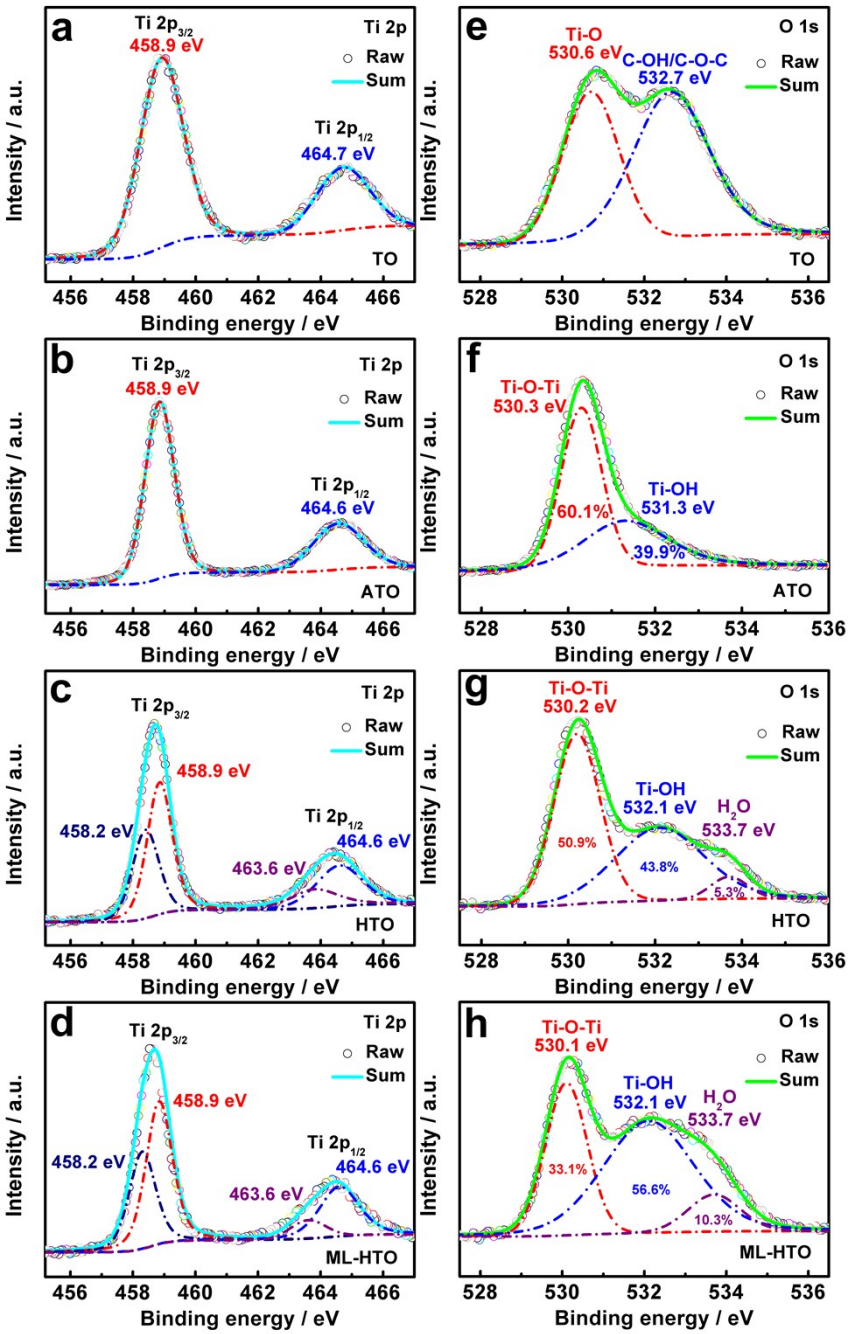

Figure S3 Deconvoluted peaks of (a-d) the Ti 2p core level XPS spectra and (e-h) the O1s core level XPS spectra of the pristine TO, ATO, HTO and ML-HTO electrodes.

As shown in **Figure S3c** and **S3d**, the deconvoluted peaks of 458.2 eV and 458.9 eV in Ti $2p_{3/2}$ peak, as well as the 463.6 eV and 464.7 eV in Ti $2p_{1/2}$ peak are observed in the HTO and ML-HTO electrodes, which should assigned to the Ti^{3+} and Ti^{4+} species, respectively. For comparison, the doublets located at 458.9 eV and 464.7

eV, only assigned to the Ti^{4+} species of the spin-orbital splitting Ti $2p_{3/2}$ and Ti $2p_{1/2}$, are observed in the active materials of the pristine TO and ATO electrodes (**Figure S3a** and **S3b**). These results indicate that the oxygen vacancy defects (Ti^{3+}) are derived from the hydrogenation process. The ratios of the Ti^{3+} and Ti^{4+} species in the total Ti species based on the integration of the deconvoluted peaks in the TO, ATO, HTO and ML-HTO electrodes are given in **Table S1**. As shown, the ML-HTO electrode exhibits the highest Ti^{3+} ratio, corresponding to the highest content of oxygen vacancy defects. As shown in **Figure S3g-S3h and Table S1**, The deconvoluted peaks of the O 1s spectra assigned to Ti-O-Ti, Ti-OH and adsorbed H_2O are observed in the ML-HTO and HTO electrodes. The surface hydroxyl groups (Ti-OH) with high content in the ML-HTO (56.6 %) and HTO (43.8%) electrodes formed during the hydrogenation process can improve the surface hydrophily of the ML-HTO and HTO electrodes. The deconvoluted peaks assigned to the adsorbed water (533.7 eV) are observed in the ML-HTO and HTO electrodes, confirming their high surface hydrophily. For comparison, low content of Ti-OH groups is observed in the ATO (39.9 %) electrode. Moreover, only deconvoluted peaks assigned to the Ti-O and residual carbon species from melamine are observed in the pristine TO electrode. These results indicate the improvement of the surface hydrophily of the ML-HTO and HTO electrodes after hydrogenation process.

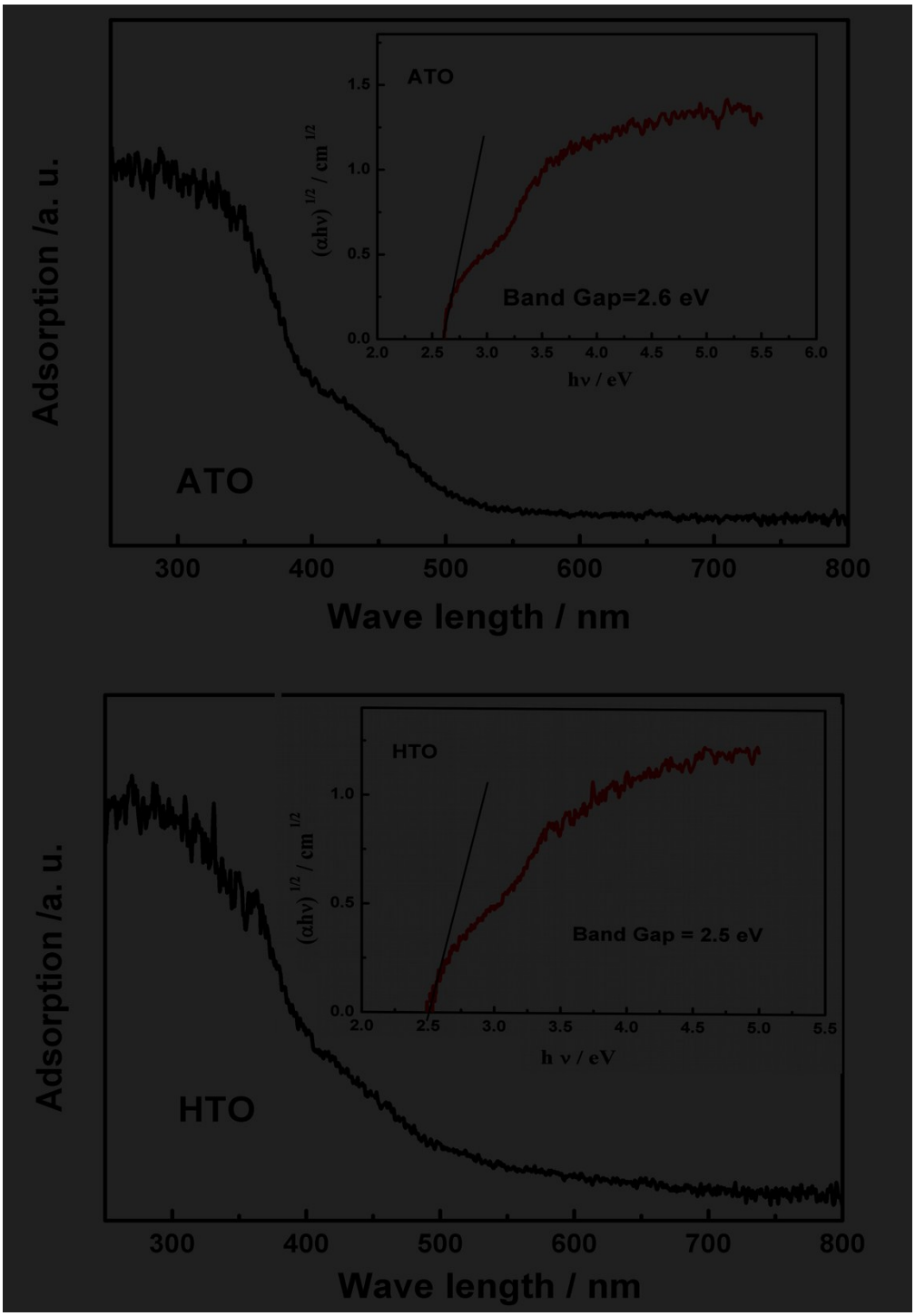

Figure S4 UV-visible adsorption spectra and Tauc plots (insets) of the (a) ATO and (b) HTO electrodes

As shown **Figure S4**, clear adsorption edges are observed in the UV-visible diffusion reflectance spectra of the ATO and HTO electrodes, indicating their semi-conductor characteristics. The band gap calculated via Tauc plots (insets of **Figure S4**)

of the ATO and HTO electrodes are 2.6 eV and 2.5 eV, respectively. Due to the TiO_2-II phase structure of ATO with little impurity, the band gap of TiO_2-II phase may be 2.6 eV. The narrowing of band gap in HTO (2.5 eV) and ML-HTO (2.39 eV) should be ascribed the oxygen vacancy defects formed during the hydrogenation process.

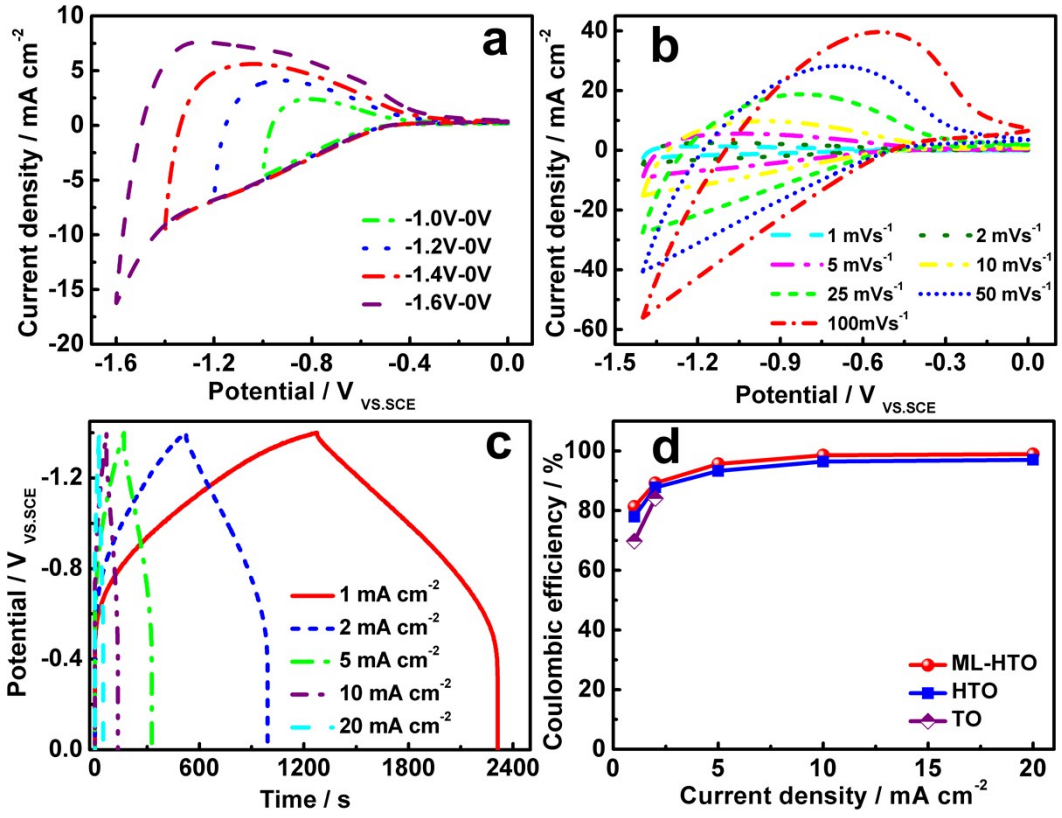

Figure S5 (a) CV curves of the ML-HTO electrode at different potential ranges at the scan rate of 5 mV s^{-1}, (b) CV curves of the ML-HTO electrode at different scan rates (c) Charge/discharge curves of the ML-HTO electrode at different current densities, (d) Coloumbic efficiency of the TO, HTO, ML-HTO electrodes at different charge/discharge current densities.

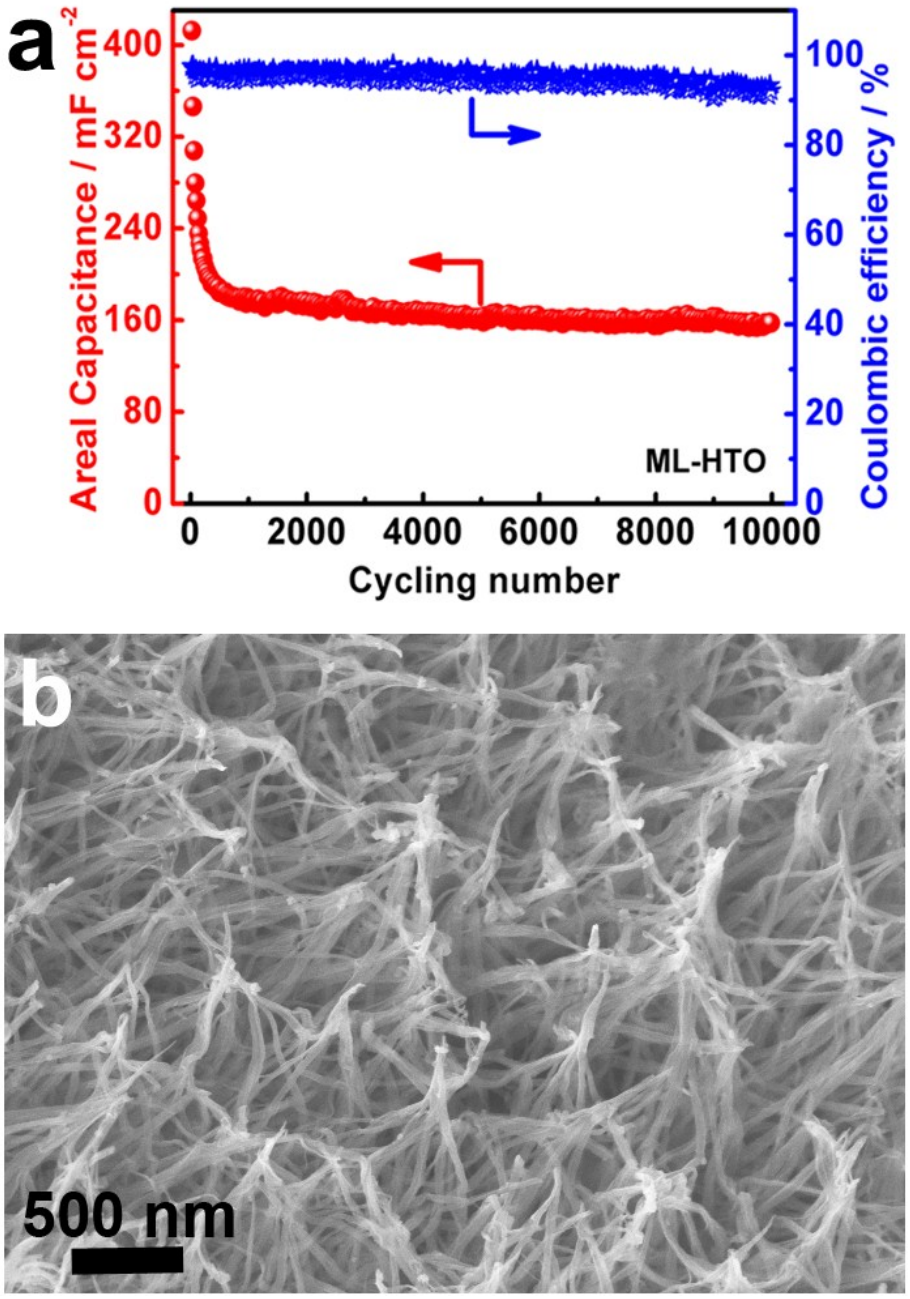

Figure S6 (a) Cycle performance of the ML-HTO electrode at 5.0 mA cm^{-2}, (b) SEM image of the ML-HTO electrode from overhead view after 10000 charge/discharge cycles.

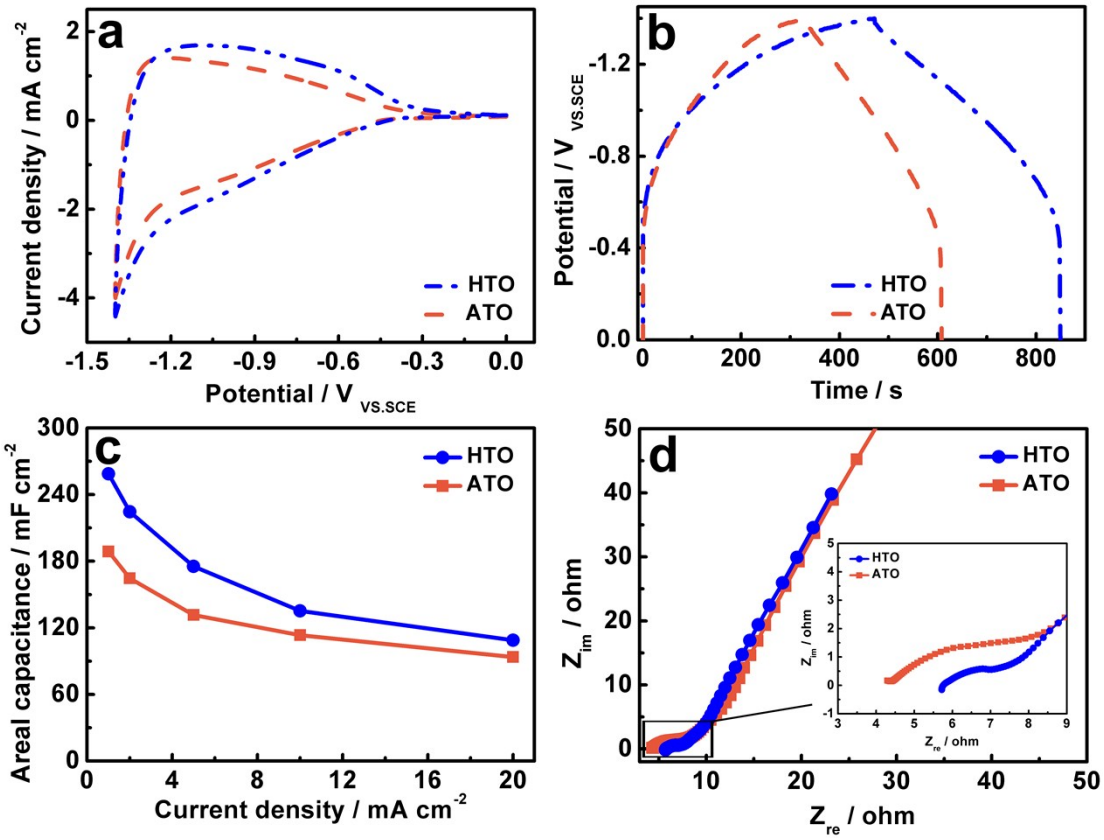

Figure S7 (a) CV curves of HTO and ATO electrodes at 5.0 mV s^{-1}, (b) Charge/discharge curves of HTO and ATO electrodes at 1.0 mA cm^{-2}, (c) Areal specific capacitance of HTO and ATO electrodes at different current densities, (d) EIS spectra of HTO and ATO electrodes.

Discussions: As shown in **Figure S7a** and **S7b**, the HTO electrode exhibits higher area for the CV curve and longer charge/discharge time for charge/discharge curves, corresponding to its higher specific capacitance than that of the ATO electrode. **Figure S7c** exhibits the higher specific capacitances at different current densities of the HTO electrode (258.7, 224.5, 175.4, 135.3 and 108.8 mF cm^{-2} at 1.0, 2.0, 5.0, 10 and 20 mA cm^{-2}, respectively) than that of the ATO electrode (188.7, 164.6, 131.7, 113.4 and 93.7 mF cm^{-2} at 1.0, 2.0, 5.0, 10 and 20 mA cm^{-2}, respectively). The lower

charge transfer resistance (**Figure S7d**) of the HTO electrode than that of the ATO electrode confirms the facilitation of intercalation/deintercalation of Na^+ or H^+ ions in the hydrogenated TiO_2 electrode.

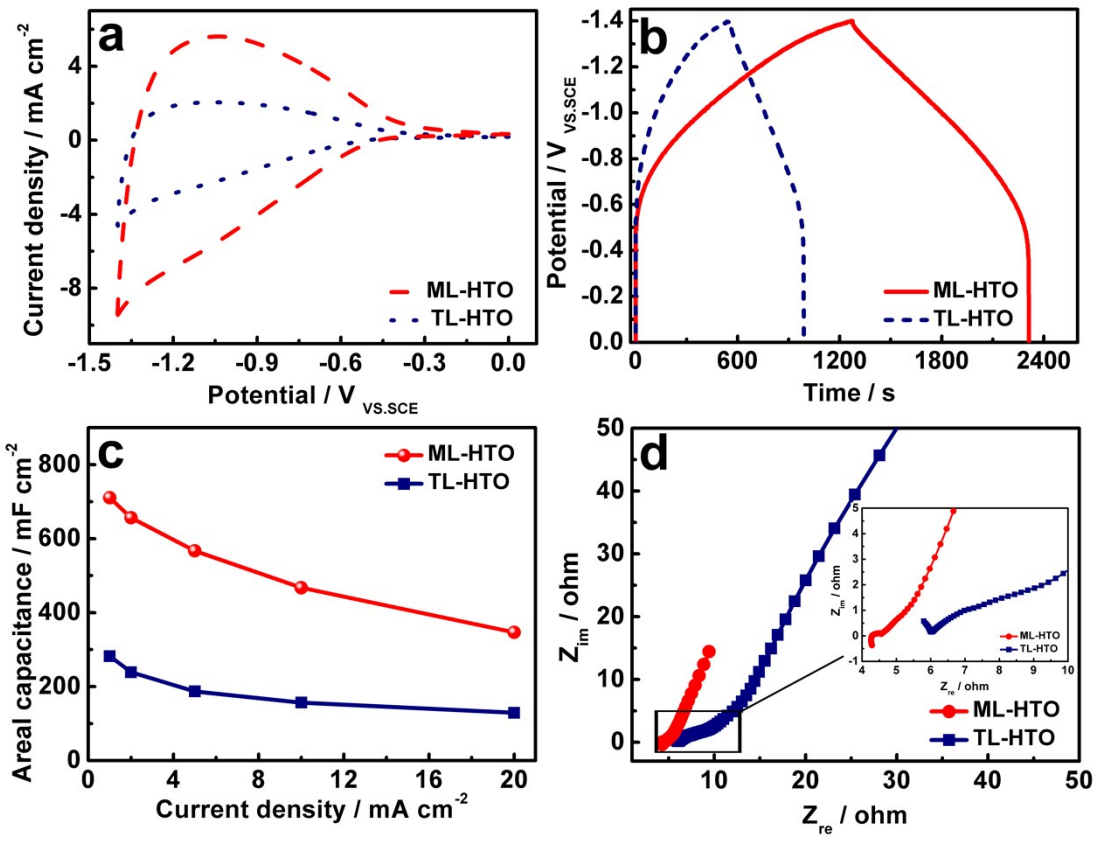

Figure S8 (a) CV curves of ML-HTO and TL-HTO electrodes at 5.0 mV s^{-1}, (b) Charge/discharge curves of ML-HTO and TL-HTO electrodes at 1.0 mA cm^{-2}, (c) Areal specific capacitance of ML-HTO and TL-HTO electrodes at different current densities, (d) EIS spectra of ML-HTO and TL-HTO electrodes.

Discussions: As shown in **Figures S8a and S8b**, the larger area of CV curve and the longer charge/discharge time for the ML-HTO electrode than that for the TL-HTO electrode indicates its higher areal specific capacitance. The areal specific capacitances of TL-HTO electrode at the current densities of 1.0, 2.0, 5.0, 10.0 and

20.0 mA cm^{-2} are 282.3, 238.9, 187.2, 156.9, 129.1 mF cm^{-2} (**Figure S8c**), respectively, which were visibly lower than those of the ML-HTO electrode, although both of their active material loadings were approximately 3.0 mg cm^{-2}. The EIS spectra (**Figure S8d**) indicates the lower ohmic resistance and charge transfer resistance of the ML-HTO electrode than that of the TL-HTO electrode. These results imply that the carbon coating transition layer can improve the electric conductive path and facilitate the charge transfer during the charge/discharge process.

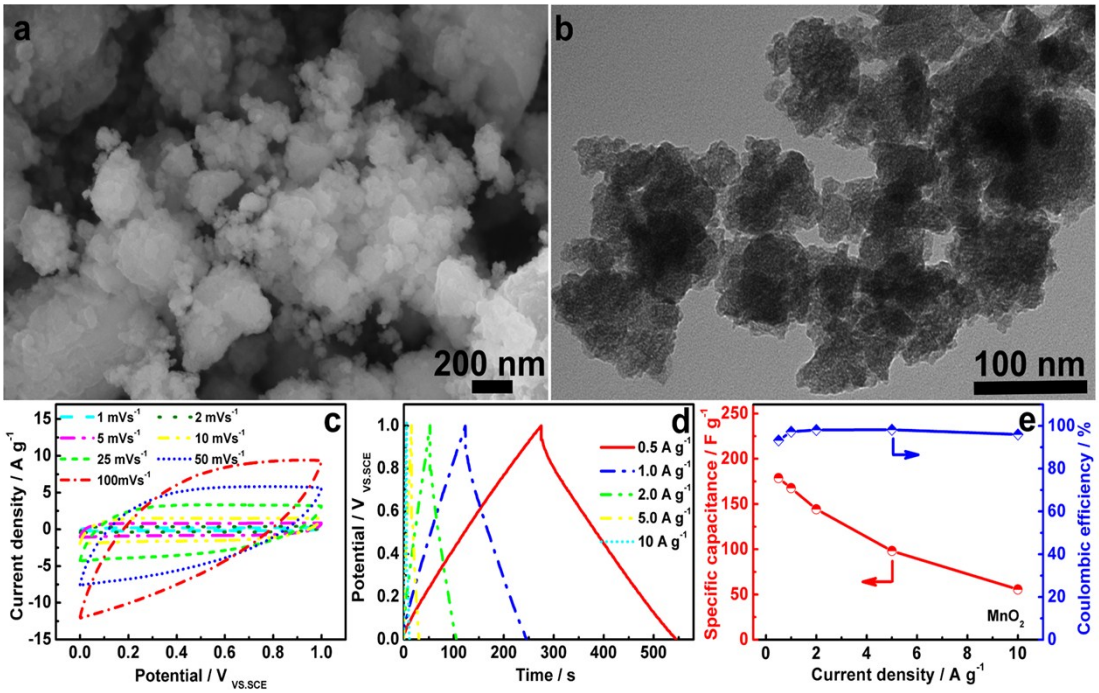

Figure S9 (a) SEM image and (b) TEM image of MnO_2 active materials, (c) CV curves of the MnO_2 coated carbon cloth electrode at different potential scan rates at the range of 0.0 ~ 1.0 V $_{vs\ SCE}$, (d) Galvanostatic charge/discharge curves at different current densities at the potential range 0.0 ~ 1.0 V $_{vs\ SCE}$, (e) Specific capacitances of the MnO_2 electrodes at different densities.

Discussions: MnO_2 nanoparticles were observed in the SEM and TEM images (**Figures S9a** and **S9b**). CV curves (**Figure S9c**) and charge/discharge curves (**Figure S9d**) of the MnO_2 electrode indicate that the MnO_2 electrode can operate at 0.0 ~ 1.0 V $_{vs\ SCE}$, implying its suitability as the positive electrodes for aqueous ASCs. The MnO_2 electrode (**Figure S9d**) exhibits high specific capacitances of 178.7, 167.6, 144.3, 98.2 and 55.6 F g^{-1} at the current density of 0.5, 1.0, 2.0, 5.0 and 10.0 A g^{-1}, respectively.

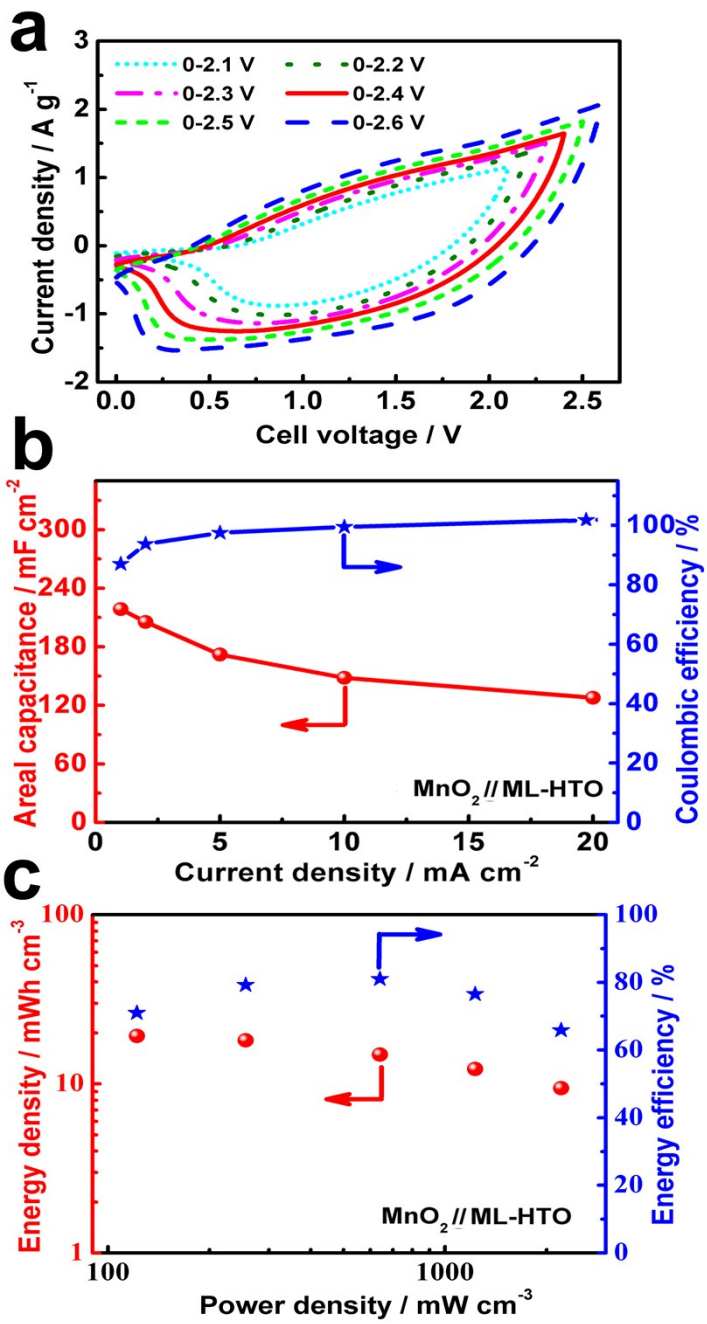

Figure S10 (a) CV curves of the MnO_2//ML-HTO ASC at different voltage windows at the potential scan rate of 10 mV s^{-1}, (b) Areal specific capacitances and Coloumbic efficiencies of the ML-HTO electrode at different current densities, (c) Volumetric energy densities of the MnO_2//ML-HTO supercapacitor at different volumetric power densities.

References

[1] K. Spektor, D. T. Tran, K. Leinenweber, U. Häussermann, Transformation of rutile to TiO_2-II in a high pressure hydrothermal environment, ***J. Solid State Chem.***, 2013, 206, 209-216.

[2] J. P. Smith, F. C. Smith, A. E. Krull-Davatzes, B. M. Simonson, Billy P. Glass, K. S. Booksh, Raman microspectroscopic mapping with multivariate curve resolution-alternating least squares (MCR-ALS) of the high-pressure, α-PbO_2-structured polymorph of titanium dioxide, TiO_2-II, ***Chin. Sci. Bull.***, 2013, 58, 4655-4662.

[3] W. Zuo, C. Xie, P. Xu, Y. Li, J. Liu, A Novel Phase-Transformation Activation Process toward Ni-Mn-O Nanoprism Arrays for 2.4 V Ultrahigh-Voltage Aqueous Supercapacitors, ***Adv. Mater.***, 2017, 29, 1703463